tvst

Glaucoma

Biological Correlations and Confounders for Quantification of Retinal Ganglion Cells by Optical Coherence Tomography Based on Studies of Outbred Mice

Adam Hedberg-Buenz[1,2], Kacie J. Meyer[2], Carly J. van der Heide[2], Wenxiang Deng[1,3], Kyungmoo Lee[3], Dana A. Soukup[2], Monica Kettelson[6], Danielle Pellack[2], Hannah Mercer[2], Kai Wang[5], Mona K. Garvin[1,3], Michael D. Abramoff[3,4,6], and Michael G. Anderson[1,2,4]

[1] VA Center for the Prevention and Treatment of Visual Loss, Iowa City VA Health Care System, Iowa City, IA, USA
[2] Department of Molecular Physiology and Biophysics, University of Iowa, Iowa City, IA, USA
[3] Department of Electrical and Computer Engineering, University of Iowa, Iowa City, IA, USA
[4] Department of Ophthalmology and Visual Sciences, University of Iowa, Iowa City, IA, USA
[5] Department of Biostatistics, University of Iowa, Iowa City, IA, USA
[6] Department of Biomedical Engineering, University of Iowa, Iowa City, IA, USA

Correspondence: Michael G. Anderson, Department of Molecular Physiology and Biophysics, 3123 Medical Education and Research Facility, 375 Newton Road, Iowa City, IA 52242, USA. e-mail: michael-g-anderson@uiowa.edu

Received: November 23, 2021
Accepted: August 2, 2022
Published: September 22, 2022

Keywords: retinal ganglion cells; optical coherence tomography; optic nerve axons; diversity outbred mice; ganglion cell complex

Citation: Hedberg-Buenz A, Meyer KJ, van der Heide CJ, Deng W, Lee K, Soukup DA, Kettelson M, Pellack D, Mercer H, Wang K, Garvin MK, Abramoff MD, Anderson MG. Biological correlations and confounders for quantification of retinal ganglion cells by optical coherence tomography based on studies of outbred mice. Transl Vis Sci Technol. 2022;11(9):17, https://doi.org/10.1167/tvst.11.9.17

Purpose: Despite popularity of optical coherence tomography (OCT) in glaucoma studies, it's unclear how well OCT-derived metrics compare to traditional measures of retinal ganglion cell (RGC) abundance. Here, Diversity Outbred (J:DO) mice are used to directly compare ganglion cell complex (GCC) thickness measured by OCT to metrics of retinal anatomy measured ex vivo with retinal wholemounts and optic nerve histology.

Methods: J:DO mice (n = 48) underwent fundoscopic and OCT examinations, with automated segmentation of GCC thickness. RGC axons were quantified from para-phenylenediamine–stained optic nerve cross-sections and somas from BRN3A-immunolabeled retinal wholemounts, with total inner retinal cellularity assessed by TO-PRO and subsequent hematoxylin staining.

Results: J:DO tissues lacked overt disease. GCC thickness, RGC abundance, and total cell abundance varied broadly across individuals. GCC thickness correlated significantly to RGC somal density (r = 0.58) and axon number (r = 0.44), but not total cell density. Retinal area and nerve cross-sectional area varied widely. No metrics were significantly influenced by sex. In bilateral comparisons, GCC thickness ($r = 0.95$), axon ($r = 0.72$), and total cell density ($r = 0.47$) correlated significantly within individuals.

Conclusions: Amongst outbred mice, OCT-derived measurements of GCC thickness correlate significantly to RGC somal and axon abundance. Factors limiting correlation are likely both biological and methodological, including differences in retinal area that distort sampling-based estimates of RGC abundance.

Translational Relevance: There are significant—but imperfect—correlations between GCC thickness and RGC abundance across genetic contexts in mice, highlighting valid uses and ongoing challenges for meaningful use of OCT-derived metrics.

Introduction

Retinal ganglion cells (RGCs) are the first neuron in the visual phototransduction circuit to fire an action potential; input from RGC dendrites is summated at the soma and projected toward the lateral geniculate nucleus in the brain via RGC axons, where it is ultimately processed into vision. Thus RGCs are critical to the physiology of vision, and damage to any part of these neurons is potentially threatening to sight. RGCs are post-mitotic, so their loss is irreversible and leads to permanent vision loss. The most common ophthalmic disease of RGCs is glaucoma,[1] but changes indicative of RGC damage are also a feature of several diseases with broader systemic effects, including diabetes,[2] Alzheimer's disease,[3] multiple sclerosis,[4,5] and some forms of traumatic brain injury,[6–9] among others.[10] Clinically assessed structural indexes of RGC damage in glaucoma have traditionally focused on features of optic nerve head morphology, such as increasing cup-to-disc ratio and the presence of notching. More recently, advances in optical coherence tomography (OCT) have made it practical to more broadly assess additional features of RGC loss, including thickness of the neuroretinal rim and thickness of the ganglion cell complex (GCC; combined thickness of areas containing the RGC axons, soma, and dendrites).[11–13]

Although OCT-derived measurements are increasingly popular metrics for RGC disease—in both humans[14,15] and animal models[16]—OCT is prone to known artifact, and some interpretations remain unclear.[17,18] One key question that has not been fully addressed is whether noninvasive OCT-derived measurements are in fact associated with biological measurements of RGC abundance made from histology-based analyses, such as quantifications from retinal wholemounts or cross-sections of the optic nerve. Existing studies that have addressed this question have tended to rely on inbred mouse models of overt disease.[19–22] Although useful in many regards, a limitation of this approach is that there would tend to be little variation in the control mice and a large difference between them and the experimental mice. Thus the strength of some correlations might be exaggerated, and other phenomena obscured. It is also well appreciated that studies comparing the thicknesses of retinal layers measured with OCT versus histologic cross-sections face a significant challenge from skews introduced during histologic sample preparation.[21] Here, we use healthy outbred mice to study the relationships of in vivo OCT-derived GCC thickness to ex vivo quantified metrics of RGC abundance. RGC number is influenced by heredity as a complex trait,[23–25] so it is expected to vary between mice with different genetic backgrounds. J:DO mice are a stock of mice with a high degree of genetic heterogeneity and therefore are expected to have a corresponding wide range of RGC abundance between individuals. Therefore this variability in RGC abundance provides a rigorous opportunity to test how changes in RGC abundance correspond to thickness of the GCC. Our overall experimental design involved acquiring a large cohort of J:DO mice, noninvasively imaging all retinas using OCT, and using automated segmentation to quantify GCC thickness. After euthanasia, we subsequently analyzed immunostained retinal wholemounts with semi-automated techniques that quantified total cellular and RGC density in the inner retina. We also quantified RGC axon number in the optic nerve. From these data, we were able to evaluate biological correlates of GCC thickness, as well as gain insight into previously unknown aspects of basic ocular anatomy and potential confounding variables relevant to RGC quantification.

Methods

Experimental Animals

Mice were maintained on a 4% fat NIH 31 diet provided as desired, housed in cages containing dry bedding (Cellu-dri; Shepherd Specialty Papers, Kalamazoo, MI, USA), and kept in a 21°C environment with a 12-hour light/12-hour dark cycle. All mice were treated in accordance with the Association for Research in Vision and Ophthalmology Statement for the Use of Animals in Ophthalmic and Vision Research. All experimental protocols were approved by the Institutional Animal Care and Use Committee of the University of Iowa.

Sample Numbers

Data were collected from all mice in an identical order, but implementation of inclusion/exclusion criteria and attrition resulted in losses such that the number of samples utilized in final data sets were not equal across all assays (Summarized in Supplementary Fig. S1). A cohort of adult Diversity Outbred mice[26] (J:DO; n = 48 mice, equal numbers of males and females, eight weeks of age) were ordered from The Jackson Laboratory (Stock no: 009376, Bar Harbor, ME, USA) and subsequently housed at the University of Iowa Research Animal Facility. A total of 15 mice died between eight and 20 weeks of age, frequently

related to anesthesia but also without apparent cause during aging; tissues from these mice were excluded from all immunohistochemical and histologic analyses. At 16 weeks of age, both eyes of 47 mice underwent OCT imaging. Scans from two mice failed quality control when later subjected to automated segmentation (described in detail below); data from both eyes of these mice were excluded from the GCC thickness dataset (leaving 45 pairs of eyes in the final GCC thickness dataset). Tissues from the two mice excluded from the GCC dataset were nonetheless carried through and contributed to the immunohistochemical and histologic analyses. One to two days after OCT imaging, the right fundus of 47 mice was imaged by fundoscopy, with one mouse (no. 15725) having developed a cloudy cornea after OCT imaging that prevented imaging (leaving 46 images in the final fundoscopy data set); mouse no. 15725 with the cloudy cornea was later found to also have a damaged optic nerve, thus the retina and optic nerve from this apparently induced unilateral anomaly were excluded. At 20 weeks of age, 33 mice were euthanized, and tissues were collected. From 33 retinas available for the left eye analysis, four were damaged in the original flat-mounting procedure and one (from mouse no. 15725) was excluded as explained above (leaving 28 retinas in the final BRN3A dataset). For unknown reasons, one of the BRN3A-labeled retinas was insufficiently stained by TO-PRO (leaving 27 retinas in the final TO-PRO dataset). When these same retinas were later stained with hematoxylin and eosin (H&E) another six succumbed to stresses of processing (i.e., retinas became delaminated or fractured into smaller pieces) and were unable to be analyzed (leaving 22 retinas in the left eye H&E dataset). From 33 retinas available for the right eye analysis, six became damaged at the time of flat-mounting (leaving 27 in the final right eye H&E dataset). From 66 optic nerves, both nerves of two mice were inadvertently lost during dissection or processing, and one (from mouse no. 15725) was excluded as explained above (leaving 61 optic nerves, 30 pairs, in the final paraphenylenediamine [PPD] dataset). When data were excluded for the reasons described above, it was done so by an investigator masked to other data for that sample; no samples were excluded based on the appearance of being an outlier in the final graphs.

Spectral Domain OCT Imaging and Analysis

Mice were anesthetized with a mixture of ketamine (87.5 mg/kg VetaKet; Akorn, Lake Forest, IL, USA) and xylazine (12.5 mg/kg AnaSed Injection; Akorn) by intraperitoneal injection, and corneas were kept lubricated with balanced salt solution (Alcon Laboratories, Fort Worth, TX, USA). Anesthetized mice were placed onto an adjustable cassette connected to a platform to allow three-dimensional movement (referred to as "OCT" hereafter; Bioptigen Envisu R2200; Bioptigen, Inc., Morrisville, NC, USA). OCT scanning was centered on the optic nerve head of the retina and aligned in the horizontal and vertical planes.[2] Scan parameters were as follows: rectangular volume scans 1.4 mm in diameter, 400 A-scans/B-scan, 400 B-scans/volume, 1 frame/B-scan, and 1 volume. Following imaging, mice were administered yohimbine (2 mg/kg of body weight; Yobine Injection; Akorn), provided supplemental indirect warmth for anesthesia recovery, and eyes were hydrated with ointment (Artificial Tears; Akorn), as described previously.[27] Previous independent studies have demonstrated the reproducibility of using OCT scans for measurement of retinal thickness[28] and in its application to studies in the mouse eye.[29]

Offline automated segmentation was performed using the Iowa Reference Algorithms 4.0 for three-dimensional automated layer segmentation; the thickness of the GCC was quantified as the distance between the upper surface of the inner limiting membrane and bottom surface of the inner plexiform layer.[30,31] A circular area (diameter = 0.2 mm) centered on the optic nerve head was used to exclude area around the nerve from measurement. An independent validation has shown favorable performance of this algorithm in comparison to other known algorithms for the inner retina in mice.[32] Quality control was performed on all segmentations and consisted of two independent steps. First, using a series of objective exclusion criteria, image scans were omitted from analyses if three of the four metrics were satisfied: quality index < 11.9,[33] maximum tissue contrast index < 10.4,[34] (RetMinCost, unitless) $> 33{,}181$, or duration of analysis (RetTime, in seconds) > 312. Exclusion cutoffs for these metrics were set at two standard deviations above (retMinCost, RetTime) or below (maximum tissue contrast index) the mean for all retinal scans. This first layer led to the exclusion of two volumetric scans, one from each of two mice. As a second layer of quality control, an observer (K.L.) blinded to the study design and animal subjects, visually inspected automated layer segmentations in all B-scans to identify those with potential segmentation errors and exclude them from layer thickness measurements. This identified a total of $n = 29$ volumetric or retinal scans (31%; 29/94 total volumes) with segmentation errors, wherein 157 ± 70 B-scans (mean $\pm$ SD; 39% = 157/400 B-scans per volume) were excluded from each of the $n = 29$ volumes that had been identified. Most segmentation errors involved the algorithm mistakenly recognizing focal areas of the

posterior surface of the lens (specifically, the inverted "ghost-image" of the lens) as an inner retinal surface, resulting in confined errors.

Fundus Imaging

Pupils were dilated using a combination of 2% cyclopentolate hydrochloride ophthalmic solution (Cyclogyl; Alcon Laboratories) and 2.5% phenylephrine hydrochloride ophthalmic solution (Paragon BioTeck, Inc., Portland, OR, USA). Once pupils were fully dilated, mice were anesthetized with a mixture of ketamine (87.5 mg/kg; VetaKet) and xylazine (12.5 mg/kg; AnaSed Injection) by intraperitoneal injection, and corneas were kept lubricated with balanced salt solution (Alcon Laboratories, Fort Worth, TX, USA). After anesthesia administration, hypromellose 2.5% ophthalmic demulcent solution (Goniovisc; HUB Pharmaceuticals, LLC, Rancho Cucamonga, CA, USA) was applied to each eye. Right eyes were imaged with a Micron III retinal imaging microscope (Phoenix Research Labs, Pleasanton, CA, USA). After imaging, mice were administered yohimbine (2 mg/kg of body weight; Yobine), were provided supplemental indirect warmth for anesthesia recovery, and their eyes were hydrated with ointment (Artificial Tears), as described previously.[27]

Collection of Retinas and Optic Nerves

Mice were euthanized by carbon dioxide inhalation, with death confirmed by cervical spine dislocation. Retinas were collected as previously described.[35] In brief, eyes were collected and the posterior eye cups were dissected and drop-fixed in ice-cold 4% paraformaldehyde in 1× phosphate buffered saline solution (PBS) for four hours, rinsed in PBS at 4°C, from which point, the left and right eyes from each mouse were prepared for H&E staining or BRN3A immunolabeling methodologies, respectively. Optic nerves were collected and processed for histology as previously described.[36] In brief, heads were removed from mice and submerged into half-strength Karnovsky's fixative for 24 hours and rinsed in 0.1 M sodium cacodylate at 4°C.

Preparation, Imaging, and Quantitative Analysis of Hematoxylin-Eosin Stained Retinas

Fixed retinas from the left eye of mice were processed, whole-mounted, stained with H&E, imaged, and quantitatively analyzed as previously described.[35,37] In brief, dissected and processed retinas were transferred to positively charged glass microscope slides, mounted flat, dried overnight, and stained with H&E. Two images in each concentric zone (peripheral, mid-peripheral, and central) for each of the four petals of each retina were collected (n = 24 images per retina), using a light microscope (BX52; Olympus, Tokyo, Japan) with identical camera (DP72, Olympus) and software (CellSens; Olympus) settings. Before further processing, retinal image sets were screened for quality control. For inclusion in the study: (1) eight images had to be collected from each of the three zones of concentricity (peripheral, mid-peripheral, and central) of the retina, for a total of 24 images, and (2) after the removal of artifacts (including tears, holes, and debris) from images using the RetFM-J image analysis plugin, the sum of analyzed area (termed *included area* in RetFM-J) from all 24 images combined had to exceed 85% (or 2.86 of the 3.36 mm^2) of the total retinal area sampled. Samples damaged during processing, such that 24 nonoverlapping and concentrically distributed sample areas could not be imaged, were excluded. Finally, the RetFM-J plugin was run using Fiji image analysis software[38] to segment and quantify nuclei from retinal image sets. Nuclei counted by RetFM-J were calculated as mathematical averages of nuclei across all images per retina and were expressed in terms of density.

Preparation, Imaging, and Quantitative Analysis of BRN3A Immunolabeled Retinas

Fixed posterior eye cups from the right eye of mice were permeabilized with 0.3% Triton-X 100 in PBS (PBST) overnight at 37°C. Retinas were dissected from cups and further permeabilized at -80°C for 15 min. and thawed at room temperature for 30 min. All following steps were carried out at room temperature, unless otherwise noted. Retinas were dissected and blocked with 2% normal donkey serum in PBST for three hours or overnight at 4°C. Retinas were incubated with an anti-BRN3A antibody (C-20, 1:200; Santa Cruz Biotechnology, Dallas, TX, USA) in PBS with 2% normal donkey serum, 1% Triton-X 100, and 1% dimethyl sulfoxide. Retinas were rinsed in PBST, incubated with a donkey anti-goat Alexa488-conjugated secondary antibody (A11055, 1:200; Life Technologies, Madison, WI, USA) in PBS with 5% normal donkey serum, 1% Triton-X 100, and 1% dimethyl sulfoxide, rinsed in PBST with TO-PRO-3 (abbreviated TO-PRO; Thermo Fisher Scientific, Waltham, MA, USA), mounted with Aqua-Mount (Lerner, Pittsburgh, PA, USA), and topped with a weighted coverslip to promote flat mounting.

Immunolabeled retinas from J:DO mice were imaged using confocal microscopy (LSM710; Zeiss, Oberkochen, Germany). For each retina, images (1024 × 1024 px, 425.1 mm^2 image area) were collected at total magnification ×400 from non-overlapping fields at each zone of eccentricity of the inner retina (such that n = 12 images total; four central, four mid-peripheral, four peripheral). Retinal image sets (n = 12 images) were opened in Fiji image analysis software[38] and prepared for quantitative analysis by a stepwise method using tools available within Fiji. Each image set underwent background subtraction with rolling ball radius set to 35 pixels, smoothened, conversion to binary using Huang thresholding, object erosion with subsequent dilation, watershed thresholding, and the fill holes function. Finally, $BRN3A^+$ nuclei were segmented using the analyze particles function with a size inclusion limit of (20-150 μm^2) and circularity (0-1). Density data were presented as the mean density of $BRN3A^+$ nuclei per $mm^2 \pm$ SD for each retina. Counts of total $BRN3A^+$ RGC number were calculated by multiplying average density with area measured within each zone of eccentricity and summing the products for all three zones for each retina, as previously described.[39] Samples damaged during processing, such that 12 nonoverlapping and concentrically distributed sample areas could not be imaged, were excluded.

Preparation, Imaging, and Quantitative Analysis of Optic Nerve Axons

Mouse optic nerves were collected, processed, stained with PPD, and imaged as previously described.[40] In brief, mouse heads were collected and submerged in half-strength Karnovsky fixative; nerves were dissected and embedded in resin, histologic sections were collected using an ultramicrotome (UC6; Leica, Wetzler, Germany) equipped with a diamond knife (Histo; Diatome, Hatfield, PA, USA), and stained with PPD, which stains the myelin sheath of normal axons and the axoplasm of dead or degenerating axons.[41] Stained optic nerve sections were imaged using a light microscope (BX52; Olympus) equipped with a camera (DP72, Olympus) and corresponding software (CellSens). Before analyses, histological sections from each optic nerve were screened for quality control to ensure the plane of cutting was cross-sectional, sufficiently stained (i.e., areas within the tissue on the section that contained myelinated structures were PPD^+, whereas areas outside the tissue were PPD^- and transparent), and the embedding resin was fully polymerized throughout the tissue. If these conditions were not met, sections were discarded and replaced.

Automated quantitative analyses were performed using AxonDeep,[42] an automated image analysis tool based on an algorithm that uses deep-learning to quantify optic nerve axons.[43] Manual axon quantifications were performed by an experienced technician masked to all other data, following previously described methodology.[40] Qualitative grading of optic nerve specimens was additionally performed by three skilled technicians masked to other data who used a three-point optic nerve grading scale (increasing numerical grade with increasing damage: 1 = none to mild, 2 = moderate, 3 = severe) previously used to assess glaucomatous damage in mice.[44]

For validation of the AxonDeep[45] tool, automated counts by AxonDeep from a subset of optic nerve specimens were compared to manual axon counts. Axons were quantified from a series of images (n = 80 images) also subjected to manual quantifications that were collected from optic nerves (n = 8 nerves, one nerve from each of eight mice; 10 images per nerve) and compared using a Pearson's correlation coefficient (*r*).

Measurements of Retinal Area

Montages of whole retinas were generated by stitching together adjacent light microscopy fields (at a total magnification ×20; using the same light microscopy setup referenced above) of H&E-stained wholemounts using the Manual MIA function in CellSens image analysis software (CellSens). All retinal montages were generated using identical microscope and camera settings. Area measurements were made by manually tracing the edges of stained retinal wholemounts using the polygon tracing tool and measure function contained in Fiji image analysis software.[38] Regions of retina containing artifacts resulting from the physical manipulation of the tissue, including folds, a common occurrence in the peripheral retina, and holes, were accounted for in the measurements of retinal area. Comparisons of retinal area by sex were done using an unpaired Student two-tailed *t*-test.

In addition to area measurements of retinas from J:DO mice, retinal area was also assessed from cohorts of inbred adult DBA/2J (4 mos. and 16 to 24 mos. of age) and C57BL/6J (2 to 5 mos. and 18 to 20 mos. of age) mice. Whenever possible, measurements were made from both retinas of each mouse studied. A subset of retinas from these cohorts were part of a previously published study[39]; in the current study, archived tissue underwent additional quantitative analyses of retinal area. Mean retinal area was calculated and compared between groups of different ages within the DBA/2J and C57BL/6J cohorts using an unpaired Student two-tailed *t*-test; comparisons among all three strains within the two to five months

age group were made using an analysis of variance with a Tukey's post-hoc test for multiple corrections.

Results

Comparisons Relevant to GCC Thickness

In vivo retinal OCT images were collected (Fig. 1A) from a large cohort of J:DO mice, and automated 3D segmentation was used to measure GCC thickness (Fig. 1B). Of 45 mice, all had overtly normal-appearing retinas. Thickness of the GCC varied broadly between individuals (Fig. 1C; range 16.3 μm; mean ± SD, 62.1 ± 3.6 μm; coefficient of variation [CV] = 5.9). Within individuals, differences in GCC thickness of the left and right eye were less varied (average ratio left/right = 0.99 ± 0.01; left: range 16.0 μm; mean ± SD, 62.1 ± 3.7 μm; CV = 6.0; right: range 15.8 μm; mean ± SD, 62.2 ± 3.6 μm; CV = 5.8) and were significantly correlated to one another ($r = 0.95$, $P < 1.0E\text{-}4$; Fig. 1C). Fundus examinations showed many variations in pigmentation and vessel structure, but no indexes of spotting characteristic of many retinal degenerations, nor overt abnormalities such as colobomas indicative of developmental anomalies (Supplemental Fig. S2). After the in vivo analysis, retina and optic nerve tissues were collected for quantitative analyses of several cellular features (Figs. 2A-D). Ex vivo retinal measurements varied widely between individuals, with less variation between measurements made bilaterally in individual mice (Figs. 2E, 2F). Qualitatively, all histologic tissues appeared healthy, for example, lacking fragmented nuclei in the retinal wholemounts and optic nerves lacking notable numbers of axons with dark axoplasmic staining by PPD. Using the damage grading scale for mice, all optic nerves had a score of "1"—indicative of healthy nerves. As expected for mice with a diverse genetic background, the number of axons in the optic nerve varied widely (range 24,339–69,517 axons; mean ± SD = 53,994 ± 6,495, n = 61 optic nerves from 31 mice; CV of 12.0%).

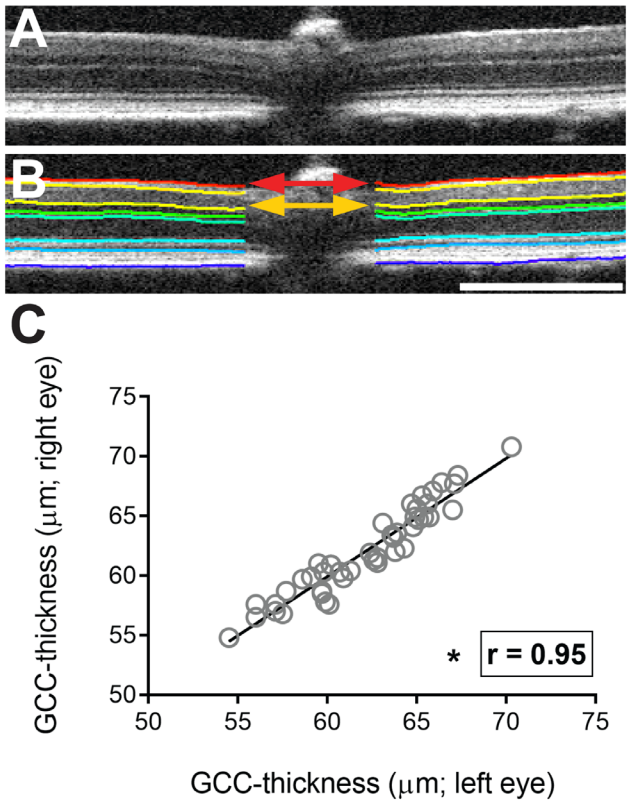

Figure 1. Retinal ganglion cell complex thickness is variable across individual J:DO mice but conserved within individuals. Image scans from in vivo retinal scans obtained by OCT, were analyzed using custom algorithms to segment and quantify thickness of retinal layers, and specifically the retinal GCC. Correlation testing of GCC thickness between the left and right eyes of the same mouse within the study cohort of J:DO mice. A representative OCT image of retina in (A) raw and (B) analyzed form. After analysis of the raw image, the analyzed form contains inset lines to denote segmentation of the different layers (by differing color) within the retina. The GCC consists of the nerve fiber, ganglion cell, and inner plexiform layers combined, and its thickness is the sum of these layers (vertical distance between *red* and *gold arrows*). *Scale bar:* 0.5 mm. (C) Graph plotting thickness of the right versus left GCC, showing a strong correlation ($r = 0.89$) of GCC thickness between eyes of the same individual in a cohort of J:DO mice. Each *dot* represents mean GCC thickness of the right (*y-axis*) versus left (*x-axis*) eye from an individual J:DO mouse (n = 45 mice, 90 retinas), *inset line* represents the best-fit line, Pearson's correlation coefficient (*r*), and the *asterisk* represents a $P < 0.05$ using a two-tailed Student *t*-test.

In vivo and ex vivo measurements were then tested for correlations to one another (Table 1). Correlations between GCC thickness and average density of total nuclei in the inner retina were insignificant, whether measured in H&E-stained (Fig. 3A) or TO-PRO-labeled (Fig. 3B) samples. In contrast, correlations of GCC thickness with RGC-specific features were greater, including both average density of BRN3A$^+$-nuclei (Fig. 3C) and number of PPD$^+$ axons in the optic nerve (Fig. 3D); both correlations were statistically significant.

A Fisher's *Z*-Transformation was performed on the Pearson's correlation coefficients to test the strength of their relationships (Table 2) before they were compared. In these comparisons, GCC thickness ($r = 0.44$) and BRN3A$^+$-based methods ($r = 0.46$) for quantifying RGC soma correlated similarly to the axon count reference standard with no significant difference between the two techniques. A similar result was obtained when the same comparison (GCC thickness: $r = 0.37$; BRN3A$^+$ density: $r = 0.45$) was done relative

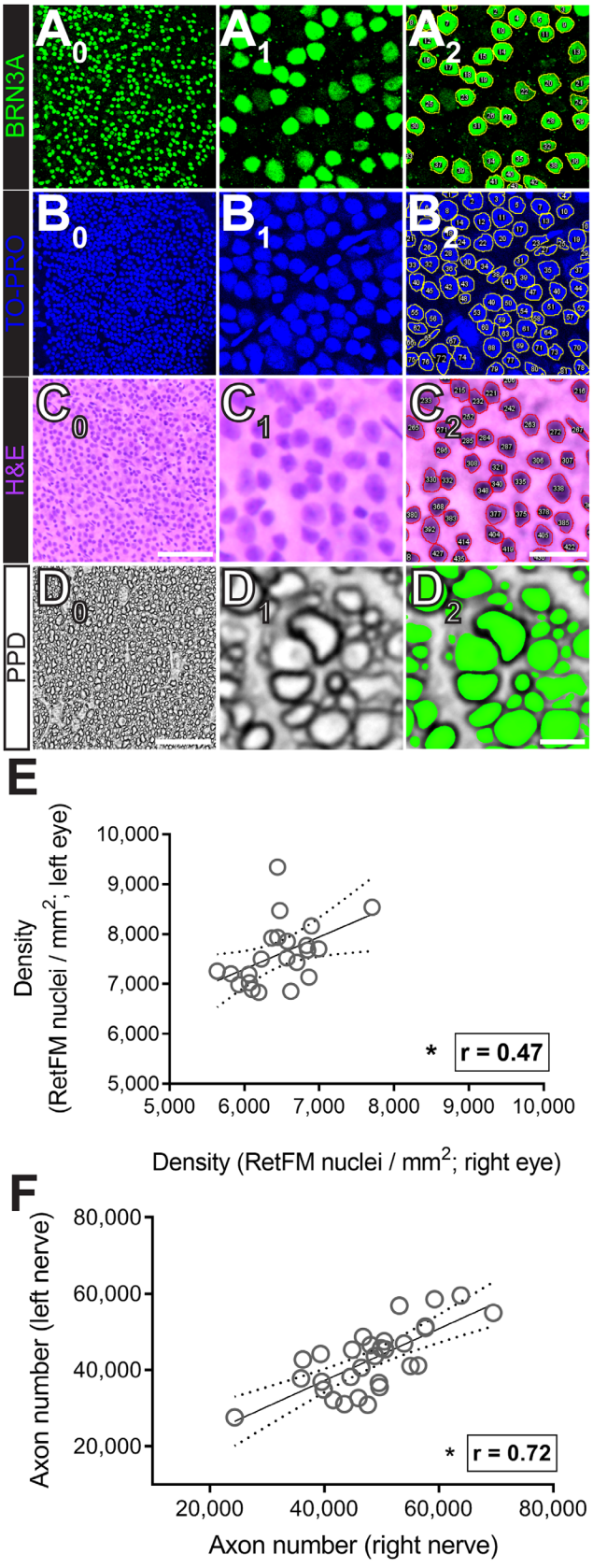

Figure 2. Quantitative analyses of neuronal features in retinas and optic nerves from J:DO mice. Representative micrographs of stained wholemount retinas and optic nerve cross-sections collected from adult J:DO mice used in quantitative analyses of neuronal features. Images in raw format (*first column, X_0*) are of native size and magnification, whereas those in analyzed format are magnified and cropped down to better enable visualization of the neuronal features, both before (*second column, X_1*) and after (*third column; features with inset contours or highlights, X_2*) analyses. Confocal micrographs acquired from the same microscopy field of retina ($A_{0\text{-}2}$) immunolabeled with an antibody targeting an RGC-specific marker (BRN3A, *in green*) and ($B_{0\text{-}2}$) counterstained with TO-PRO (*nuclei, in blue*). Light micrographs from a ($C_{0\text{-}2}$) retina stained with hematoxylin and eosin (*nuclei, violet; extracellular space, pink*) and ($D_{0\text{-}2}$) optic nerve stained with PPD (myelin sheath, black). *Scale bars:* 100 µm (A_0–C_0), 25 µm ($A_{1,2}$-$C_{1,2}$), 10 µm (D_0), and 2 µm ($D_{1,2}$). Graphs relating quantifications of (E) total nuclei density (cells/mm^2; n = 22 mice) in the inner neural layers of retina and (F) axons (extrapolated number; n = 31 mice) in optic nerve between the left and right nerves of the same individual among the population of J:DO mice. Each *dot* represents data from both retinas or nerves of one mouse, inset line represents best-fit line, Pearson's correlation coefficient (*r*), and *asterisks* represent a $P < 0.05$ using a two-tailed Student *t*-test.

to a smaller set of optic nerves (n = 8 nerves) that had also been manually counted.

In our quantitative analyses of RGC metrics, the use of complementary assays in individual eyes provided opportunities for comparing the performance of some assays. Automated and manual axon counts were highly correlated (Supplementary Fig. S3, $r = 0.94$, $P < 1.0\text{E-}4$; n = 8 optic nerves, one from each of eight mice), as were H&E- and TO-PRO-based counts of total nuclei from retinal wholemounts (Supplementary Fig. S4; central retina: $r = 0.94$, mid-peripheral retina: $r = 0.87$, peripheral retina: $r = 0.67$; $P < 6.0\text{E-}4$ for all three comparisons; $n = 22$ data pairs for each retinal zone from 22 retinas, one from each of 22 mice).

Additional Comparisons Relevant to Retinal Anatomy and its Measurement

Variability in retinal size has previously been observed with buphthalmia secondary to elevated intraocular pressure,[46] amongst some strains with different genetic backgrounds,[47] and with natural aging[48,49]—which we have replicated (Supplementary Fig. S5). In our analysis of the retinal wholemounts from these outbred J:DO mice, we observed that the size of the retina appeared to vary substantially (Fig. 4A-B). To quantify this, measurements from a subset of samples (n = 49 retinas, both from each of 27 mice) were made and total retinal area was indeed found to range from 15.0 to 26.1 mm^2 (mean ± SD; 20.3 ± 2.4 mm^2; Fig. 4C). Variation in retinal area was associated with changes in cellular density. Average densities of TO-PRO$^+$ (Fig. 4D) and BRN3A$^+$ nuclei (Fig. 4E) were both significantly correlated to retinal

Table 1. Quantitative Comparison of the Relationships (Pearson's Correlation Coefficients [*r*]) Between GCC Thickness and Abundance of RGC Somas in Retina or RGC Axons in Optic Nerve of the Same Eye and Nerve Pair From J:DO Mice

Metrics Correlated	*r*	n = Mice	n = Eyes or Nerves	Significance	*P* Value
GCC thickness with:					
Left versus right eyes	0.95	45	90	*	<1.0E-04
BRN3A$^+$ nuclei density (left)	0.58	28	28	*	1.0E-03
TO-PRO$^+$ nuclei density (left)	0.36	27	27	No	6.5E-02
RetFM-J nuclei density (both)	0.10	22	49	No	5.3E-01
Axon counts with:					
Left versus right optic nerves	0.72	31	61	*	<1.0E-04
GCC thickness (both)	0.45	29	57	*	<4.0E-04
Left eye	0.51	28	28	*	3.2E-03
Right eye	0.41	29	29	*	2.4E-02
NFL+GCL thickness (both)	0.42	29	57	*	7.0E-04
Left eye	0.40	28	28	No	6.6E-02
Right eye	0.49	29	29	*	2.2E-03
BRN3A$^+$ nuclei density (left)	0.46	26	26	*	1.9E-02
TO-PRO$^+$ nuclei density (left)	0.45	24	24	*	2.7E-02
RetFM-J nuclei density (both)	0.07	25	46	No	8.3E-01

area, smaller densities being observed in retinas with larger area ($r = -0.72$, $P < 1.0E-4$; $r = -0.65$, $P = 2.0E-4$; respectively). Using total axon number as a surrogate for total RGC number, average density of BRN3A$^+$ nuclei was also significantly correlated with RGC number (Fig. 4F), with density increasing as the number of axons increased ($r = 0.46$, $P = 1.9E-2$). Together, these observations point to a potential problem with common practices to quantify RGCs—two retinas with the same density of RGCs may or may not have a similar number of RGCs, depending on retinal area.

As a complementary approach to ascertain total RGC number, we also calculated "estimated cellular number" purely from retinal data by multiplying the area of each zone of eccentricity in the retinal wholemounts by the average density in that same zone (Supplementary Figs. S6A–C), as done previously.[39] Doing so resulted in a conversion of the average density of BRN3A$^+$ nuclei from 3117 ± 514 RGCS/mm^2 to an extrapolated 53,946.5 ± 7904.3 RGCs/retina. However, we did not detect a significant relationship between the estimated total number of BRN3A$^+$ RGCs and total axon number ($r = 0.20$; $P = 3.4E-1$, Supplementary Fig. S6D), suggesting that this method of estimating total RGC number is, at present, relatively crude. This conversion to RGC number did not improve the strength of the correlations with GCC thickness ($r = 0.50$; $P = 1.0E-2$, Supplementary Fig. S6E).

Cross-sectional area of the optic nerve also varied substantially between J:DO mice (ranging from 0.05–0.13 mm^2; mean ± SD, 0.09 ± 0.02 mm^2; n = 61 nerves; CV of 22%; Figs. 5A–G). There was a significant positive relationship between total cross-sectional area of the optic nerve and total axon number ($r = 0.57$; $P < 1.0E-4$; n = 61 optic nerves; Fig. 5H). Like the retina, increasing area of the optic nerve was associated with decreased average axon density ($r = -0.43$; $P < 1.0E-4$; n = 61 optic nerves; Fig. 5I). Average optic nerve cross-sectional area and retinal area were not significantly associated with one another (Fig. 5J).

In the inbred mouse strains that have previously been studied, it is known that displaced amacrine cells constitute a significant fraction—approximately 50.3%—of the cells in the ganglion cell layer of mice.[50] Thus RGCs are oddly a minority cell-type in the ganglion cell layer of mice. It is unknown if this fraction is relatively constant or fluctuates according to genetic background. In our data, there was a significant positive relationship between the overall cell density of BRN3A$^+$ and TO-PRO$^+$ nuclei in J:DO retinas ($r = 0.77$, $P < 1.0E-4$, Supplementary Fig. S7A). BRN3A$^+$ nuclei were 42.5% ± 4.7% (mean ± SD) of all TO-PRO$^+$ nuclei, with a range from 32 to 52% (Supplementary Fig. S7B).

There were no significant differences in any parameters studied between male and female J:DO mice (Table 3).

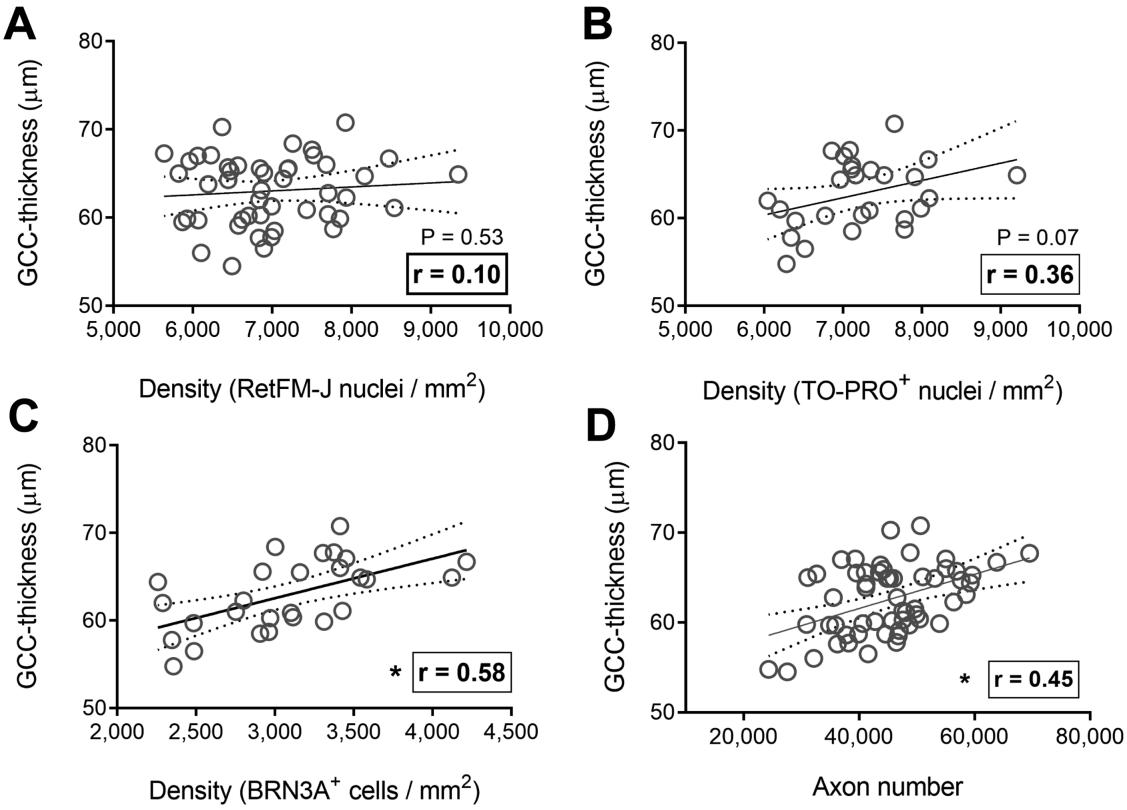

Figure 3. Relating cellular features to retinal structure in the ganglion cell complex of J:DO mice. Graphs relating how measurements of cellularity from retinal wholemounts relate to structural thickness by OCT of GCC thickness in adult J:DO mice. Dot plots showing the relationship between structural thickness of the GCC (*y-axis*) versus the overall cell density of all types residing in these layers, whether stained by (A) H&E (with analysis by RetFM-J) or (B) TO-PRO (with analyses using a custom macro for Image-J), (C) density of retinal ganglion cells (with BRN3A immunolabeling and analysis using a custom macro for Image-J), or (D) extrapolated axon number. Note that the relationship between GCC thickness and overall cell density is relatively poor and not statistically significant, whereas those with RGC density and axon number are stronger and achieve significance. Each dot represents data from both eyes or nerves (n = 47 for A and n = 48 for D) or from one eye (n = 27 for B and C) of one mouse, *inset line* represents best-fit line, Pearson's correlation coefficient (*r*), and *asterisks* represent $P < 0.05$ using a two-tailed Student *t*-test.

Table 2. Comparing the Relationship Strength (Pearson's Correlation Coefficient, r) Between GCC Thickness and RGC Somal Counts to the Manual Axon Count Reference Standard Within the Same Eye and Nerve Pair From J:DO Mice

Comparing GCC Thickness vs. $BRN3A^+$ Density	r vs. r	Test Statistic Based on the Fisher's Z-Transformation	Significant Difference	*P* Value
Relative to Axon Deep axon count	0.44 vs. 0.46	−0.10	no	4.6E-01
Relative to manual axon count	0.37 vs. 0.45	−1.52	no	4.4E-01

Discussion

Quantification of RGC abundance is an important aspect in clinical management of several diseases, and in research, it is often the cornerstone of studies using mice to study diseases of RGCs such as glaucoma. OCT-derived measurements have become popular metrics, despite some ambiguity in their biological properties. In humans and larger animals, OCT can be used to measure several features relevant to RGC health, including GCC thickness, retinal nerve fiber

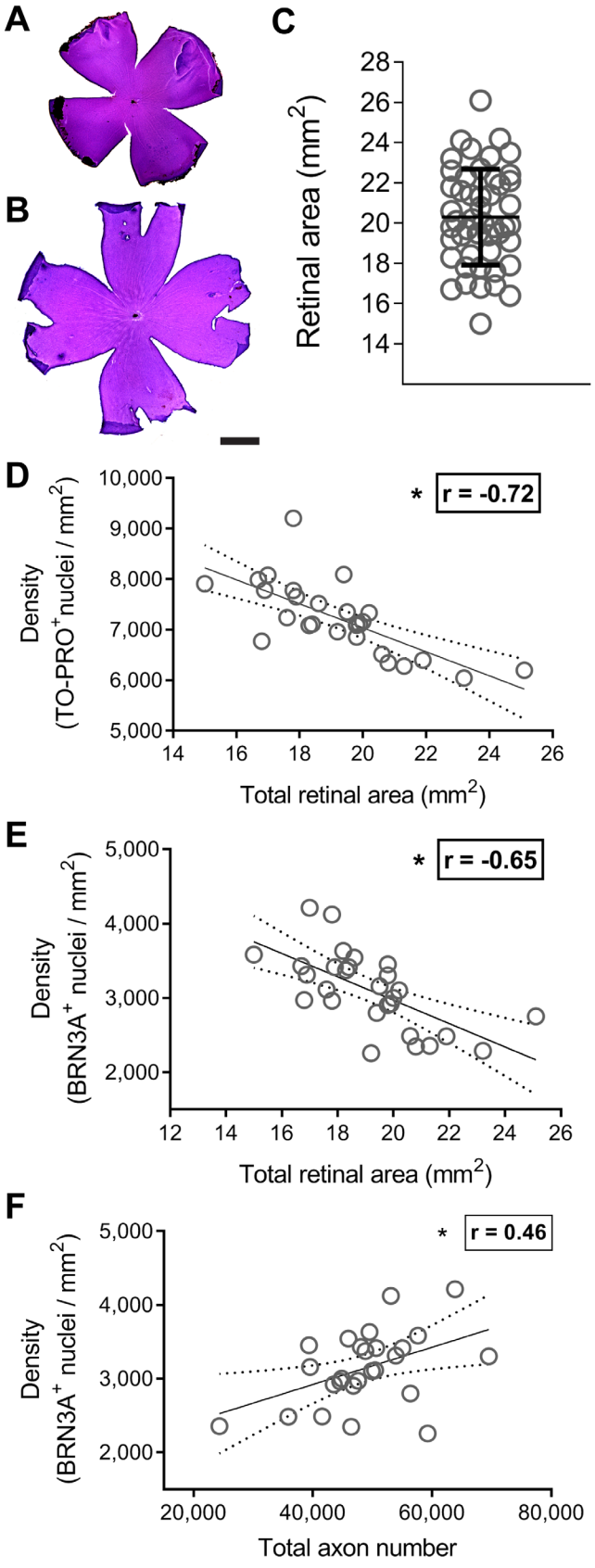

Figure 4. Relating cellular features in the ganglion cell complex to overall retinal area in J:DO mice. Image and graphical data relating how measurements of total area relate to cellular features collected from the same retinal wholemounts in adult J:DO mice. Representative light microscopy images of relatively (A) small and (B) large H&E-stained retinas collected from the J:DO cohort. *Scale bar:* 500 µm. (C) Graph showing the distribution of area measurements for all retinas (n = 49) included in the study. Each *dot* represents data from one retina, *inset horizontal* and *vertical lines* represent the mean ± SD area for all retinas, respectively. Dot plots relating the (D) density of TO-PRO$^+$ nuclei and (E) density of BRN3A$^+$ nuclei versus retinal area, respectively, and (F) density of BRN3A$^+$ nuclei versus total axon number. Each *dot* represents data from the left eye/nerve pair from one mouse (n = 27 pairs for D; n = 28 pairs for E and F), *inset solid* and *dotted lines* represent the best-fit and 95% confidence interval, respectively, Pearson's correlation coefficient (*r*), and *inset asterisk* to represent a $P < 0.05$ using a two-tailed Student *t*-test.

layer thickness, and optic nerve head morphology, among others. The comparatively small size of the mouse eye challenges reliable measurement of some of these tissues, leading us and others to use GCC thickness. Here, we have characterized retinal features of outbred J:DO mice and experimentally tested the degree to which OCT-derived measurements of GCC thickness may be correlated to total cellular density in the RGC layer, RGC density, and axon number in the optic nerve. The results indicate that there are indeed significant—but imperfect—correlations between GCC thickness and RGC abundance across a wide range of values in mice. Our analyses also uncovered or confirmed several features relevant to the basic biology of RGCs and their quantification.

This study compared in vivo OCT measurements of GCC thickness to direct ex vivo measurements made with dissected tissues of the same eyes—an experiment that would obviously be impractical in humans. The results found confirmatory evidence that GCC thickness correlates positively to RGC abundance. While several studies analyzed mouse retinas with both OCT and RGC-specific immunostaining,[51–54] relatively few have tested the correlations between these measurements.[4,55] Nishioka and colleagues[4] studied correlations between RGC density determined by immunostaining with RBPMS[56] and OCT-derived GCC thickness in mice with experimental autoimmune encephalomyelitis. After eight weeks of disease, a context in which RGC density had decreased by 23.3% and the remaining RGC somas had shrunk in cross sectional area by 27.4%, there was a significant correlation with GCC thickness ($r = 0.759$, $P < 0.0001$), which was slightly improved if baseline GCC thickness was considered and "GCC thinning" used instead. Likewise, Ho and colleagues[55] compared histologically determined numbers of total cells in the ganglion cell layer from sampling of retinal cross-sections with OCT-derived measurements of GCC thickness in mice

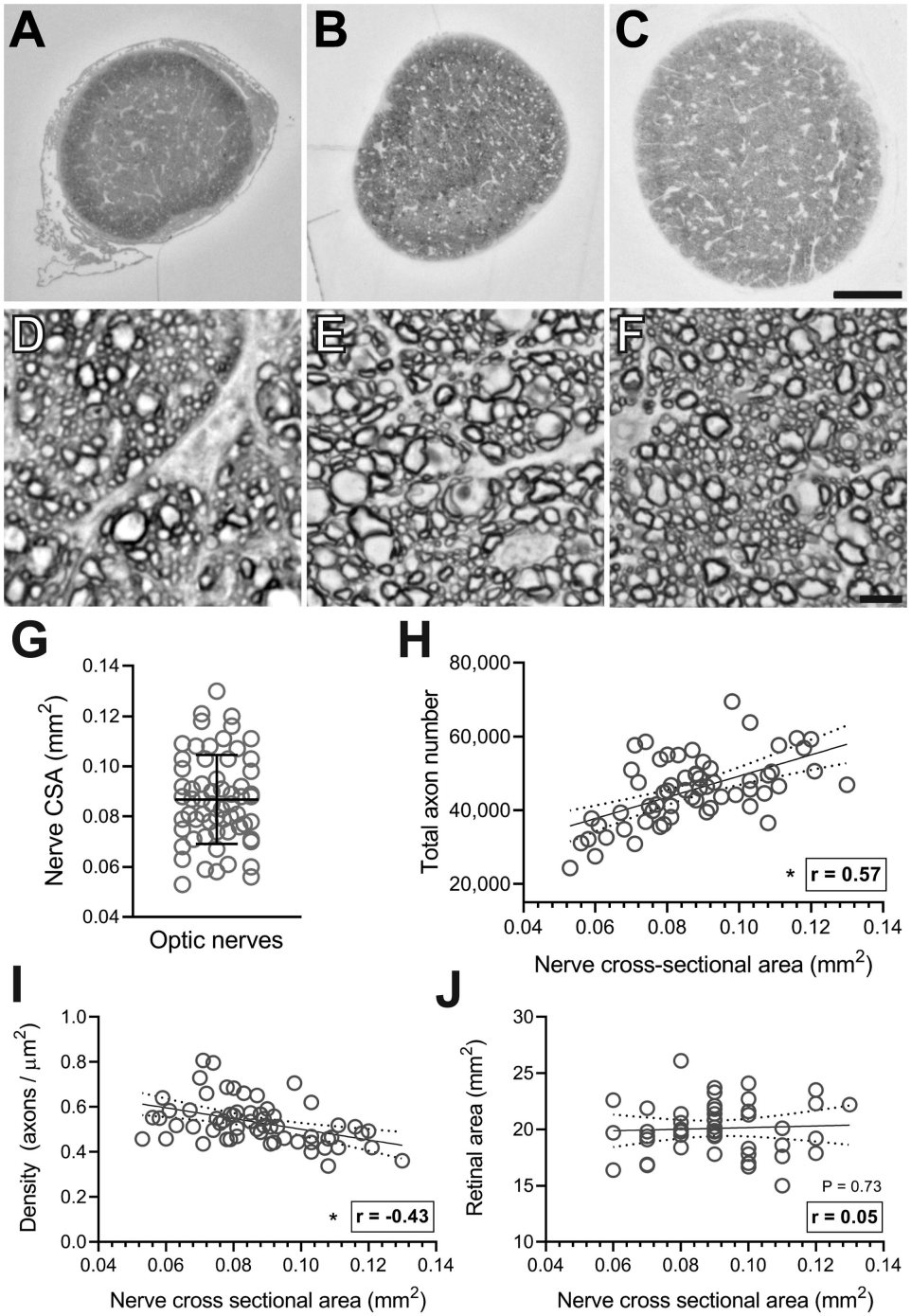

Figure 5. Relating variability in axon number with optic nerve structure in J:DO mice. Light micrograph pairs of PPD-stained optic nerve cross-sections of three representative optic nerves, presented in their entirety (*top row*) and magnified (*bottom row*), collected from adult J:DO mice. These micrographs were collected from optic nerves with the (A, D) smallest, (B, E) median, and (C, F) largest cross-sectional areas in the study cohort. *Scale bars:* 100 µm (total magnification ×100; A–C) and 5 µm (×1000; D–F). (G) Graph showing the distribution of cross-sectional area (CSA) measurements for all nerves included in the study. Each *dot* represents data from one nerve, *inset horizontal* and *vertical lines* represent the mean ± SD area for all nerves, respectively. *Dot plots* relating (H) total axon number, (I) mean axon density, and (J) retinal surface area to the CSA of the corresponding optic nerve. Each *dot* represents data from one optic nerve (n = 61) or nerve/retina pair (as in J; n = 46), *inset solid* and *dotted lines* represent the best-fit and 95% confidence interval, respectively, Pearson's correlation coefficient (*r*), and *asterisks* represent $P < 0.05$ using a two-tailed Student *t*-test.

Table 3. Cellular and Structural Features of Retina and Optic Nerves in Male Versus Female J:DO Mice

Parameter	Male		Female		Significant Difference	*P* Value
	Mean ± SD	No.	Mean ± SD	No.		
NFL + GCL thickness	15.3 ± 0.7 µm	46	15.3 ± 0.7 µm	44	No	8.2E-01
GCC thickness	61.8 ± 3.7 µm	46	62.6 ± 3.6 µm	44	No	2.9E-01
Optic nerve axon number	45,844.6 ± 8316.7 axons	41	44,894.2 ± 10,672.4 axons	20	No	7.0E-01
Optic nerve CSA	0.09 ± 0.02 µm^2	41	0.08 ± 0.02 µm^2	20	No	2.4E-01
RetFM nuclei density	6992.2 ± 864.5 nuclei/mm^2	34	6860.1 ± 688.5 nuclei/mm^2	15	No	6.0E-01
TO-PRO$^+$ nuclei	7369.2 ± 755 nuclei/mm^2	16	6969.8 ± 583.1 nuclei/mm^2	10	No	1.6E-01
BRN3A$^+$ density	3095.5 ± 538.3 nuclei/mm^2	17	3098.4 ± 502.9 nuclei/mm^2	11	No	9.9E-01
Retinal area	20.3 ± 2.2 µm^2	34	20.3 ± 2.8 µm^2	15	No	9.5E-01

with experimental anterior ischemic optic neuropathy. Both assays showed an initial retinal swelling, which was followed by atrophy. At four weeks after injury, a time point in which 49.3% of cells in the ganglion cell layer had been lost, there was substantial correlation between cell numbers and GCC thickness ($r^2 = 0.74$). The degree of correlation detected in these studies was higher than the analogous correlation detected in our current study ($r = 0.58$, $P = 1.0$E-3), likely because of differences in the experimental context—especially using inbred mice with induced disease versus outbred mice with only natural variation. It is also notable that both studies detected acute *increases* in GCC thickness during initial stages of disease, which only later gave way to *decreases* in GCC. With respect to methodology, this illustrates how different stages of a disease might confound interpretations based solely on GCC thickness. For example, if a disease process was not temporally synchronous, as in these induced models, then the concurrent swelling and tissue loss in slightly different areas of the inner retina might lead to off-setting changes in GCC thickness.

In humans, correlations with OCT-derived metrics in the macula have been studied using models that estimate macular RGC number.[57,58] In a study of 77 healthy, 154 suspect, and 159 glaucomatous eyes, Zhang et al. found that average thickness of the ganglion cell plus inner plexiform layer at the macula (mGCIPL thickness) was significantly correlated with the estimated number of macular RGCs ($r^2 = 0.67$; $P < 0.001$). One reason for the less than perfect correlation in this study, that was considered by the authors and is also relevant to our current study, is that the ganglion cell layer also has displaced amacrine cells that contribute to GCC thickness in a manner not directly related to RGC number. In mice, the relative ratios of RGCs, displaced amacrine cells, and other cell-types in the ganglion cell layer varies among publications with different approaches reporting that RGCs are 36.1% to 67.5% of the neurons in the ganglion cell layer.[59–61] A thorough study by Schlamp et al.[50] used retrograde labeling to derive a percentage of 50.3%, whereas the estimate from using BRN3A as a marker of RGCs yielded an estimate of 44.8% in inbred C57BL/6J mice. Our current study found that 42.5% of the total cells in the ganglion cell layer were BRN3A$^+$ RGCs, which is very similar to the findings of Schlamp et al.[50]—especially considering that Schlamp used nuclear morphology to exclude some cells from the denominator (RGCs/total neurons) whereas we included all cells (RGCs/total cells). A relevant new finding of our study was that even with a segregating genetic background, RGC and total cell densities were significantly correlated to one another in the ganglion cell layer, with only modest variation in their ratio (Supplementary Fig. S7). However, our study detected only modest correlations between total cell density and GCC thickness, presumably indicating that the predominant contribution to GCC thickness is specifically from RGCs—a finding that is supported by the fact that the GCC contains not only their somas similarly to other cells, but also includes the dendrites and axons of RGCs. Therefore mouse studies performed in a context in which genetic backgrounds are not matched should expect that RGC abundance, total cell abundance (including displaced amacrine cells), and GCC thickness would all be likely to vary substantially at baseline in different mice, but that longitudinal studies of GCC thickness over time would predominantly reflect changes to RGCs.

The J:DO stock was generated by crosses between 144 early generation recombinant inbred lines contributing to the Collaborative Cros,[62] and thus incorporates similar genetic variation, including variation from all of the major phylogenetic branches present in laboratory mice (including wild-derived CAST, PWK, WSB, and five additional standard inbred strains, such as C57BL/6J). The genetic diversity of the stock can't be maintained by traditional husbandry used in individual laboratories; the complex breeding scheme requires them to be acquired from The Jackson Laboratory. J:DO mice were developed to promote genetic analysis of complex traits[63,64] and because it is sometimes desirable to perform studies in animals that, like most humans, are not inbred. Our study shows that if overt retinal disease occurs in J:DO mice, it is likely rare (<1 in 47 mice), but that there is a broad range of variability in many retinal features that could be studied using quantitative genetics.[9] The finding that GCC thickness, total inner retinal cell density, and total axon number, were each highly correlated between the left and right tissues of individual mice, but varied widely between different J:DO mice, emphasizes that these traits likely have genetic underpinnings that could either be mapped or exploited in gene expression studies as others have done in mouse studies of myopia.[65] The phenotypic diversity of retinal phenotypes in J:DO mice also illustrate why outbred mice, or any strain with a segregating (non-inbred) genetic background, can be problematic–there is a larger probability of confounding genotypes that could lead to spurious results if comparisons are made between small experimental and control cohorts.

The finding that retinal and optic nerve cross sectional areas can naturally vary so dramatically has an important implication to studies that rely on measurements of RGC density (i.e., changes in retinal/optic nerve area and RGC number might be confused with one another). Because neither RGC number nor cross-sectional area of the retina/optic nerve are constant, a difference in density lacks meaning without a concurrent measurement of their tissue area. Because the variability of retinal cross-sectional area of outbred J:DO mice is large compared to inbred young DBA/2J or C57BL/6J mice (see Supplementary Fig. S5), it is likely that the variation in tissue sizes is genetic background dependent. Accordingly, any experiment in which the genetic background of cohorts being compared was not identical would be at risk for this confounding possibility. Some studies have used cross sectional area of the optic nerve as an indication of disease severity, which may be meaningful for models such as the DBA/2J model of glaucoma,[66] but our results caution against this approach for experiments in which genetic background is not isogenic. The apparent continuous nature of variability in tissue areas implies multigenic influences, making relevant genetic background matching between cohorts even harder. This same problem can also influence inbred mice, as illustrated by increases in retinal area that occur with natural aging (Supplementary Fig. S5)[49] and buphthalmia associated with elevated intraocular pressure in DBA/2 mice[46]—both of which alone could decrease RGC density and lead to exaggerated estimates of glaucomatous RGC loss. Based on these findings, we suggest that all studies of RGC abundance made using density measurements also report the tissue areas.

Aside from genetic background,[67] sex is another relevant biological variable that should be considered in mouse studies. Although sex could influence many other physiological or pathological events, we found that sex had no significant effects on the anatomical parameters of the inner retina measured in this study. Others have previously reported that there are sex-specific differences in retinal gene expression in mice, including in microglial and RGC-specific pathways,[68] and some glaucoma studies using mice have detected sex-specific differences in disease—which would seemingly be unrelated to the traits we have studied.

The current study has multiple caveats that warrant mention. First, although RGC abundance was measured in several complementary ways, the stains and antibodies used might have influenced some results. Axons were identified by the uptake of PPD, which stains the myelin sheath of healthy axons and the axoplasm of dead or degenerating axons. Because of its lipophilic nature, PPD only stains myelinated axons. Thus our analyses were limited to myelinated axons and did not include unmyelinated axons. Likewise, the use of BRN3A as a marker of RGCs may have left some fraction of RGCs unlabeled. Among markers of RGCs, the reason we chose to use BRN3A is that it labels only the nucleus of RGCs, creating succinct regions of interest that automated imaging-based approaches can better distinguish in comparison to markers such as RBPMS, which is cytoplasmic.[56] The fraction of RGCs not labeled by BRN3A in rodents is not precisely known; studies based on immunostaining with rat wholemounts suggest it labels 96.2% of RGCs defined by retrograde labeling with FluoroGold (FG), if FG^+ microglia are discounted,[69] or 87.9% if they are not.[70] In mice, various studies have reported that BRN3A labels 81.6% of $RBPMS^+$ cells[56] and 85.6% of FG^+ cells.[71] More recent analyses using single cell RNA sequencing have found that BRN3A-encoding RNA appears to be found in all sub-classes of mouse RGCs (albeit, at varying levels).[72,73] We have

previously found that 92.8% of RBPMS$^+$ cells co-label with BRN3A in retinas of normal C57BL/6J mice.[74] In sum, BRN3A appears to be present in a high percentage of RGCs, but any RGCs not detected by BRN3A immunolabeling could have confounded our analyses. Future iterations of this type of quantitative analysis of RGC somas may benefit from simultaneous application of an antibody targeting an RGC-specific marker coupled with retrograde labeling of the soma by way of the axon. Second, we have used semi-automated quantification approaches, which confer many advantages, but are undoubtedly still imperfect. Although it is promising that the tools we are using can detect associations such as left-right eye correlations in individual mice, it's possible that some associations have been blurred by a combination of methodologic shortcomings. This challenge is illustrated in the comparison of total axon number versus total BRN3A$^+$ cell number (Supplementary Fig. S6D), which should logically be significantly correlated, but our study was unable to demonstrate. In this instance, it is likely that the sampling to calculate abundance, as opposed to counting every soma and axon throughout the entirety of these tissues, added distortion. Third, we anticipate that both OCT imaging for mice and approaches for automated quantifications of tissues will continue to evolve in the years to come. Thus the confirmation that changes detected in RGCs via OCT are indeed significantly correlated with actual anatomical changes is important, but the degree of correlation currently detected may represent a "lower limit" that will improve through technological advances in the years to come. Finally, these analyses were performed in healthy mice with sources of variation that are natural, as opposed to disease-related. As illustrated by the discussion of experimental autoimmune encephalomyelitis, it is likely that some disease processes will increase the discordance between OCT- and histologic-based measurements. The influence of age also remains to be tested.

Future iterations of this type of study may consider modifications to the experimental design and techniques used herein. First, repetitive imaging and measurement of retinal layers by OCT scans could provide insight to how static or dynamic retinal layer thicknesses are, as opposed to once per eye in this study. However, counter-balancing this modification is the potential influence of repeat anesthesia sessions that would also warrant consideration. Second, narrowing the duration of time between completion of the in vivo imaging assays and ex vivo histological assays, would reduce the potential for changes in these tissues to occur. Third, we experienced a larger than expected attrition of J:DO mice, which suggests that a further consideration of anesthesia protocols would be appropriate.

In conclusion, we have characterized several quantitative phenotypes of RGCs, including GCC thickness, density of RGCs in the retina, and axon number in the optic nerve, that exist among outbred J:DO mice. This initial characterization indicates that J:DO mice are free of overt retinal disease but have many ocular traits which vary widely between different individuals. Thus J:DO mice are a powerful resource for studies such as ours—those that rely on maximal degrees of natural phenotypic diversity—and for future studies that employ quantitative genetic approaches to investigate these types of naturally occurring diversity that exist amongst individuals within a species. Of the phenotypic correlations tested, the most important finding was that non-invasive OCT-derived measurements of GCC thickness are significantly correlated with RGC abundance measured from histology-based analyses of retina and optic nerve. By extension, these results are consistent with a hypothesis that in human, OCT-derived measurements are likely also as valid as histologic quantifications of the retina. For mouse studies, our current results also indicate that tissue area is a potentially confounding variable in studies of RGC density; that the fraction of RGCs to displaced amacrine and other cells is relatively uniform, even if RGC abundance is not; and that there were no sex-specific differences in the RGC-related metrics measured.

Acknowledgments

Supported by the US Department of Veterans Affairs Rehabilitation Research and Development (RR&D, I01RX001481) and National Institutes of Health NEI (R01EY017673) grants to MGA. MDA is supported by the Robert C. Watzke endowed Professorship, and AHB was supported by Training Grant T32 DK112751-01. We also acknowledge an NIH/NEI Center Support Grant to the University of Iowa (P30EY025580). The contents do not represent the views of the U.S. Department of Veterans Affairs or the U.S. Government.

Disclosure: **A. Hedberg-Buenz**, None; **K.J. Meyer**, None; **C.J. van der Heide**, None; **W. Deng**, None; **K. Lee**, None; **D.A. Soukup**, None; **M. Kettelson**, Digital Diagnostics, Inc. (E, I); **D. Pellack**, None; **H. Mercer**, None; **K. Wang**, None; **M.K. Garvin**, approach used to segment retinal layers (P); **M.D. Abramoff**, Digital Diagnostics Inc. (F, I, C, P); **M.G. Anderson**, None

References

1. Weinreb RN, Aung T, Medeiros FA. The pathophysiology and treatment of glaucoma: a review. *JAMA*. 2014;311:1901–1911.
2. Sohn EH, van Dijk HW, Jiao C, et al. Retinal neurodegeneration may precede microvascular changes characteristic of diabetic retinopathy in diabetes mellitus. *Proc Natl Acad Sci USA*. 2016;113:E2655–2664.
3. Dehabadi MH, Davis BM, Wong TK, Cordeiro MF. Retinal manifestations of Alzheimer's disease. *Neurodegener Dis Manag*. 2014;4:241–252.
4. Nishioka C, Liang HF, Barsamian B, Sun SW. Sequential phases of RGC axonal and somatic injury in EAE mice examined using DTI and OCT. *Mult Scler Relat Disord*. 2019;27:315–323.
5. Walter SD, Ishikawa H, Galetta KM, et al. Ganglion cell loss in relation to visual disability in multiple sclerosis. *Ophthalmology* .2012;119:1250–1257.
6. Dutca LM, Stasheff SF, Hedberg-Buenz A, et al. Early detection of subclinical visual damage after blast-mediated TBI enables prevention of chronic visual deficit by treatment with P7C3-S243. *Invest Ophthalmol Vis Sci*. 2014;55:8330–8341.
7. Mohan K, Kecova H, Hernandez-Merino E, Kardon RH, Harper MM. Retinal ganglion cell damage in an experimental rodent model of blast-mediated traumatic brain injury. *Invest Ophthalmol Vis Sci*. 2013;54:3440–3450.
8. Boehme NA, Hedberg-Buenz A, Tatro N, et al. Axonopathy precedes cell death in ocular damage mediated by blast exposure. *Sci Rep*. 2021;11:11774.
9. Harper MM, Boehme N, Dutca LM, Anderson MG. The retinal ganglion cell response to blast-mediated traumatic brain injury is genetic background dependent. *Invest Ophthalmol Vis Sci*. 2021;62:13.
10. Levin LA, Gordon LK. Retinal ganglion cell disorders: types and treatments. *Prog Retin Eye Res*. 2002;21:465–484.
11. Lee K, Kwon YH, Garvin MK, Niemeijer M, Sonka M, Abramoff MD. Distribution of damage to the entire retinal ganglion cell pathway: quantified using spectral-domain optical coherence tomography analysis in patients with glaucoma. *Arch Ophthalmol*. 2012;130:1118–1126.
12. Renard JP, Fenolland JR, Giraud JM. Glaucoma progression analysis by spectral-domain optical coherence tomography (SD-OCT). *J Fr Ophtalmol*. 2019;42:499–516.
13. Tatham AJ, Medeiros FA. Detecting structural progression in glaucoma with optical coherence tomography. *Ophthalmology*. 2017;124:S57–S65.
14. Mwanza JC, Budenz DL. New developments in optical coherence tomography imaging for glaucoma. *Curr Opin Ophthalmol*. 2018;29:121–129.
15. Chan NCY, Chan CKM. The use of optical coherence tomography in neuro-ophthalmology. *Curr Opin Ophthalmol*. 2017;28:552–557.
16. Fortune B. In vivo imaging methods to assess glaucomatous optic neuropathy. *Exp Eye Res*. 2015;141:139–153.
17. Chen JJ, Kardon RH. Avoiding clinical misinterpretation and artifacts of optical coherence tomography analysis of the optic nerve, retinal nerve fiber layer, and ganglion cell layer. *J Neuroophthalmol*. 2016;36:417–438.
18. Smith CA, Vianna JR, Chauhan BC. Assessing retinal ganglion cell damage. *Eye (London, England)*. 2017;31:209–217.
19. Yang Q, Cho KS, Chen H, et al. Microbead-induced ocular hypertensive mouse model for screening and testing of aqueous production suppressants for glaucoma. *Invest Ophthalmol Vis Sci*. 2012;53:3733–3741.
20. Ohno Y, Makita S, Shimazawa M, Tsuruma K, Yasuno Y, Hara H. Thickness mapping of the inner retina by spectral-domain optical coherence tomography in an N-methyl-D-aspartate-induced retinal damage model. *Exp Eye Res*. 2013;113:19–25.
21. Camp AS, Ruggeri M, Munguba GC, et al. Structural correlation between the nerve fiber layer and retinal ganglion cell loss in mice with targeted disruption of the Brn3b gene. *Invest Ophthalmol Vis Sci*. 2011;52:5226–5232.
22. Li L, Huang H, Fang F, Liu L, Sun Y, Hu Y. Longitudinal morphological and functional assessment of RGC neurodegeneration after optic nerve crush in mouse. *Front Cell Neurosci*. 2020;14:109.
23. Williams RW, Strom RC, Rice DS, Goldowitz D. Genetic and environmental control of variation in retinal ganglion cell number in mice. *J Neurosci*. 1996;16:7193–7205.
24. Williams RW, Strom RC, Goldowitz D. Natural variation in neuron number in mice is linked to a major quantitative trait locus on Chr 11. *J Neurosci*. 1998;18:138–146.
25. Strom RC, Williams RW. Cell production and cell death in the generation of variation in neuron number. *J Neurosci*. 1998;18:9948–9953.

26. Churchill GA, Airey DC, Allayee H, et al. The Collaborative Cross, a community resource for the genetic analysis of complex traits. *Nat Genet*. 2004;36:1133.
27. Koehn D, Meyer KJ, Syed NA, Anderson MG. Ketamine/xylazine-induced corneal damage in mice. *PLoS One*. 2015;10:e0132804.
28. Budenz DL, Chang RT, Huang X, Knighton RW, Tielsch JM. Reproducibility of retinal nerve fiber thickness measurements using the stratus OCT in normal and glaucomatous eyes. *Invest Ophthalmol Vis Sci*. 2005;46:2440–2443.
29. Gabriele ML, Ishikawa H, Schuman JS, et al. Reproducibility of spectral-domain optical coherence tomography total retinal thickness measurements in mice. *Invest Ophthalmol Vis Sci*. 2010;51:6519–6523.
30. Abràmoff MD, Garvin MK, Sonka M. Retinal imaging and image analysis. *IEEE Rev Biomed Eng*. 2010;3:169–208.
31. Antony BJ, Jeong W, Abramoff MD, Vance J, Sohn EH, Garvin MK. Automated 3D segmentation of intraretinal surfaces in SD-OCT volumes in normal and diabetic mice. *Trans Vis Sci & Technol*. 2014;3:8–8.
32. Dysli C, Enzmann V, Sznitman R, Zinkernagel MS. Quantitative analysis of mouse retinal layers using automated segmentation of spectral domain optical coherence tomography images. *Transl Vis Sci Technol*. 2015;4:9.
33. Stein DM, Ishikawa H, Hariprasad R, et al. A new quality assessment parameter for optical coherence tomography. *Br J Ophthalmol*. 2006;90:186–190.
34. Huang Y, Gangaputra S, Lee KE, et al. Signal quality assessment of retinal optical coherence tomography images. *Invest Ophthalmol Vis Sci*. 2012;53:2133–2141.
35. Hedberg-Buenz A, Christopher MA, Lewis CJ, et al. RetFM-J, an ImageJ-based module for automated counting and quantifying features of nuclei in retinal whole-mounts. *Exp Eye Res*. 2016;146:386–392.
36. Mao M, Hedberg-Buenz A, Koehn D, John SW, Anderson MG. Anterior segment dysgenesis and early-onset glaucoma in nee mice with mutation of Sh3pxd2b. *Invest Ophthalmol Vis Sci*. 2011;52:2679–2688.
37. Hedberg-Buenz A, Christopher MA, Lewis CJ, et al. Quantitative measurement of retinal ganglion cell populations via histology-based random forest classification. *Exp Eye Res*. 2016;146:370–385.
38. Schindelin J, Arganda-Carreras I, Frise E, et al. Fiji: an open-source platform for biological-image analysis. *Nat Methods*. 2012;9:676–682.
39. Hedberg-Buenz A, Christopher MA, Lewis CJ, et al. Quantitative measurement of retinal ganglion cell populations via histology-based random forest classification. *Exp Eye Res*. 2016;146:370–385.
40. Trantow CM, Mao M, Petersen GE, et al. Lyst mutation in mice recapitulates iris defects of human exfoliation syndrome. *Invest Ophthalmol Vis Sci*. 2009;50:1205–1214.
41. Smith RS, John SW, Nishina PM, Sundberg JP. *Systematic Evaluation of the Mouse Eye: Anatomy, Pathology, and Biomethods*. Boca Raton: CRC Press; 2001.
42. Deng W, Hedberg-Buenz A, Soukup DA, et al. AxonDeep: Automated Optic Nerve Axon Segmentation in Mice With Deep Learning. *Transl Vis Sci Technol*. 2021;10:22.
43. Anderson MG, Hedberg-Buenz A, van der Heide C, Meyer K, Lee K, Abramoff MD. Correlation of retinal ganglion cell metrics made in vivo using SD-OCT versus ex vivo using quantitative histology in Diversity Outbred mice. *Invest Ophthalmol Vis Sci*. 2019;60:5604–5604.
44. Anderson MG, Libby RT, Gould DB, Smith RS, John SW. High-dose radiation with bone marrow transfer prevents neurodegeneration in an inherited glaucoma. *Proc Natl Acad Sci USA*. 2005;102:4566–4571.
45. Deng W, Hedberg-Buenz A, Soukup DA, et al. AxonDeep: Automated Optic Nerve Axon Segmentation in Mice with Deep Learning. *Transl Vis Sci Technol*. 2021;10(14):22.
46. Danias J, Lee KC, Zamora MF, et al. Quantitative analysis of retinal ganglion cell (RGC) loss in aging DBA/2NNia glaucomatous mice: comparison with RGC loss in aging C57/BL6 mice. *Invest Ophthalmol Vis Sci*. 2003;44:5151–5162.
47. Raven MA, Stagg SB, Reese BE. Regularity and packing of the horizontal cell mosaic in different strains of mice. *Vis Neurosci*. 2005;22:461–468.
48. Nadal-Nicolás FM, Vidal-Sanz M, Agudo-Barriuso M. The aging rat retina: from function to anatomy. *Neurobiol Aging*. 2018;61:146–168.
49. Samuel MA, Zhang Y, Meister M, Sanes JR. Age-related alterations in neurons of the mouse retina. *J Neurosci*. 2011;31:16033–16044.
50. Schlamp CL, Montgomery AD, Mac Nair CE, Schuart C, Willmer DJ, Nickells RW. Evaluation of the percentage of ganglion cells in the ganglion cell layer of the rodent retina. *Mol Vis*. 2013;19:1387–1396.
51. Zhao D, Wong VH, Nguyen CT, et al. Reversibility of Retinal Ganglion Cell Dysfunction From

Chronic IOP Elevation. *Invest Ophthalmol Vis Sci*. 2019;60:3878–3886.

52. Dailey WA, Drenser KA, Wong SC, et al. Norrin treatment improves ganglion cell survival in an oxygen-induced retinopathy model of retinal ischemia. *Exp Eye Res*. 2017;164:129–138.
53. Hadj-Saïd W, Froger N, Ivkovic I, et al. Quantitative and topographical analysis of the losses of cone photoreceptors and retinal ganglion cells under taurine depletion. *Invest Ophthalmol Vis Sci*. 2016;57:4692–4703.
54. Stankowska DL, Dibas A, Li L, et al. Hybrid compound SA-2 is neuroprotective in animal models of retinal ganglion cell death. *Invest Ophthalmol Vis Sci*. 2019;60:3064–3073.
55. Ho JK, Stanford MP, Shariati MA, Dalal R, Liao YJ. Optical coherence tomography study of experimental anterior ischemic optic neuropathy and histologic confirmation. *Invest Ophthalmol Vis Sci*. 2013;54:5981–5988.
56. Rodriguez AR, de Sevilla Müller LP, Brecha NC. The RNA binding protein RBPMS is a selective marker of ganglion cells in the mammalian retina. *J Comp Neurol*. 2014;522:1411–1443.
57. Zhang C, Tatham AJ, Weinreb RN, et al. Relationship between ganglion cell layer thickness and estimated retinal ganglion cell counts in the glaucomatous macula. *Ophthalmology*. 2014;121:2371–2379.
58. Zhang C, Tatham AJ, Weinreb RN, et al. Relationship between ganglion cell layer thickness and estimated retinal ganglion cell counts in the glaucomatous macula. *Ophthalmology*. 2014;121:2371–2379.
59. Li Y, Semaan SJ, Schlamp CL, Nickells RW. Dominant inheritance of retinal ganglion cell resistance to optic nerve crush in mice. *BMC Neurosci*. 2007;8:19.
60. Quigley HA, Cone FE, Gelman SE, et al. Lack of neuroprotection against experimental glaucoma in c-Jun N-terminal kinase 3 knockout mice. *Exp Eye Res*. 2011;92:299–305.
61. Li Y, Semaan SJ, Schlamp CL, Nickells RW. Dominant inheritance of retinal ganglion cell resistance to optic nerve crush in mice. *BMC Neurosci*. 2007;8:19.
62. Threadgill DW, Miller DR, Churchill GA, de Villena FP. The collaborative cross: a recombinant inbred mouse population for the systems genetic era. *ILAR*. 2011;52:24–31.
63. Saul MC, Philip VM, Reinholdt LG, Center for Systems Neurogenetics of Addiction,Chesler EJ. High-diversity mouse populations for complex traits. *Trends Genet*. 2019;35:501–514.
64. Churchill GA, Gatti DM, Munger SC, Svenson KL. The Diversity Outbred mouse population. *Mamm Genome*. 2012;23:713–718.
65. Tkatchenko TV, Shah RL, Nagasaki T, Tkatchenko AV. Analysis of genetic networks regulating refractive eye development in collaborative cross progenitor strain mice reveals new genes and pathways underlying human myopia. *BMC Med Genomics*. 2019;12:113.
66. Williams PA, Harder JM, Cardozo BH, Foxworth NE, John SWM. Nicotinamide treatment robustly protects from inherited mouse glaucoma. *Commun Integr Biol*. 2018;11:e1356956.
67. Meyer KJ, Anderson MG. Genetic modifiers as relevant biological variables of eye disorders. *Hum Mol Genet*. 2017;26:R58–R67.
68. Du M, Mangold CA, Bixler GV, et al. Retinal gene expression responses to aging are sexually divergent. *Mol Vis*. 2017;23:707–717.
69. Nadal-Nicolas FM, Jimenez-Lopez M, Sobrado-Calvo P, et al. Brn3a as a marker of retinal ganglion cells: qualitative and quantitative time course studies in naive and optic nerve-injured retinas. *Invest Ophthalmol Vis Sci*. 2009;50:3860–3868.
70. Mead B, Thompson A, Scheven BA, Logan A, Berry M, Leadbeater W. Comparative evaluation of methods for estimating retinal ganglion cell loss in retinal sections and wholemounts. *PLoS One*. 2014;9:e110612.
71. Galindo-Romero C, Aviles-Trigueros M, Jimenez-Lopez M, et al. Axotomy-induced retinal ganglion cell death in adult mice: quantitative and topographic time course analyses. *Exp Eye Res*. 2011;92:377–387.
72. Rheaume BA, Jereen A, Bolisetty M, et al. Single cell transcriptome profiling of retinal ganglion cells identifies cellular subtypes. *Nat Commun*. 2018;9:2759.
73. Tran NM, Shekhar K, Whitney IE, et al. Single-cell profiles of retinal ganglion cells differing in resilience to injury reveal neuroprotective genes. *Neuron*. 2019;104:1039–1055. e1012.
74. van der Heide CJ, Meyer KJ, Hedberg-Buenz A, et al. Quantification and image-derived phenotyping of retinal ganglion cell nuclei in the nee mouse model of congenital glaucoma. *Exp Eye Res*. 2021;212:108774.